Journal of Nuclear Materials 294 (2001) 256–266

journal of nuclear materials

www.elsevier.nl/locate/jnucmat

Characterization of plastic deformation in a disk bend test

T.S. Byun *, E.H. Lee, J.D. Hunn, K. Farrell, L.K. Mansur

Oak Ridge National Laboratory, Metal and Ceramics Division, Building 5500, P.O. Box 2008, MS-6151, Oak Ridge, TN 37831, USA

Received 11 September 2000; accepted 22 January 2001

Abstract

A disk bend test technique has been developed to study deformation mechanisms as well as mechanical properties. In the disk bend test, a transmission electron microscopy (TEM) disk size specimen of 3 mm diameter ×0.25 mm thick is clamped around its rim in a circular holder and indented with a tungsten carbide ball of 1 mm diameter on its back face. AISI 316LN austenitic stainless steel and 9Cr–2WVTa ferritic/martensitic steel were selected as test materials. A model was developed to determine the average plastic strain and surface plastic strain in the disk bend test. The deformation regimes of the plastic strain versus deflection curves corresponded to those of the load versus deflection curves. The stress state of the disk bend deformation was analyzed for the two test materials and compared with those of other mechanical tests such as uniaxial tensile, compact tension, and ball indentation tests. Slip line features at the deformed surface and the corresponding TEM microstructures were examined for both tensile and disk bend specimens. Differences and similarities in deformation between the disk bend and the tensile tests are described. © 2001 Elsevier Science B.V. All rights reserved.

1. Introduction

In the past, miniaturized test techniques using thin disks or square platelets have been developed for extracting mechanical property information from a limited volume of test material [1–14]. In those techniques central loading with a ball (sometimes a rod with a flat or hemispherical tip) is applied to deform specimens and to derive load–deflection curves. Indeed, those techniques have been effectively used in providing key mechanical properties, such as strength and ductility [2,7,8,13,14], fracture toughness [9,12], and ductile–brittle transition temperature (DBTT) [10,11]. Various shapes and sizes of thin specimens have been tried in those miniaturized test techniques. Of those, the most common type has been transmission electron microscopy (TEM) disks of 3 mm diameter [1–6]. This is mainly for two reasons: (a) the same size specimens can be used in parallel studies of microstructures by TEM and (b) its small volume minimizes the total radioactivity after irradiation. Moreover, it is a standardized specimen shape, and thus preparing and handling procedures are already well developed.

Although the disk bend test has been frequently used to obtain mechanical properties, it has been seldom used for the purpose of deformation mechanism studies. Recently, a disk bend test technique has been applied to the study of deformation mechanisms for ion-irradiated AISI 316LN stainless steel [15]. TEM disks were bent by indentation loading with a tungsten carbide (WC) ball after ion-irradiation. The results demonstrated that radiation effects on plastic deformation could be economically studied by using the TEM disk bend test technique.

In the present paper, a method is developed to calculate the average and surface plastic strains of the deformed TEM disks. Since the method supplies a capability of evaluating surface plastic strain, it is used to calculate the plastic strain level in the damaged layer produced by ion-irradiation and disk bend deformation for optical and TEM examinations. The deformation regimes of the disk bend test are characterized in view of the plastic strain versus deflection curves. An analytical model is also proposed to evaluate the stress fields and stress state in the central region of disk

---

* Corresponding author. Tel.: +1-423 576 7738; fax.: +1-423 574 0641.

E-mail address: byunts@ornl.gov (T.S. Byun).

0022-3115/01/$ - see front matter © 2001 Elsevier Science B.V. All rights reserved.
PII: S0022-3115(01)00484-6

specimens. This stress analysis model is applied to two test materials, AISI 316LN stainless steel and 9Cr–2WVTa ferritic/martensitic steel, and the results are compared with the data obtained for other mechanical tests. Optical and TEM examinations were carried out for 316LN stainless steel after ion-irradiation and disk bend deformation to aid the understanding of the deformation behavior under disk bend and uniaxial tensile tests. One of the purposes of this paper is also to suggest the disk bend test as a substitute for the uniaxial tensile tests for studying deformation mechanisms.

2. Experimental

AISI 316LN austenitic stainless and 9Cr–2WVTa ferritic/martensitic steels were selected as test materials. The chemical compositions of the steels are shown in Table 1. TEM disks of 3 mm diameter were punched out of 0.25 mm thick cold-rolled sheets. Both sides of the TEM disks were ground with 600 grit emery paper before heat treatment. The 316LN stainless steel samples were annealed at 1050°C for 30 min in vacuum and fast cooled. The 9Cr–2WVTa steel samples were annealed at 1050°C for 30 min in vacuum, fast cooled to room temperature, and then tempered at 750°C for 1 h. To prepare an optically flat and scratch free surface, one side of the heat-treated TEM disk was additionally polished using 0.1 μm diamond paste followed by electrochemical polishing. Tensile specimens were also prepared in a similar manner for the purpose of comparison. The gage section dimensions of the tensile specimens were 0.25 mm in thickness ×1.5 mm in width ×7.5 mm in length.

Disk bend tests were performed in a specimen holder shown schematically in Fig. 1 using a Tinius–Olsen testing machine. The specimen holder consists of a die with a central hole of 1.6 mm diameter and a clamping screw with a central hole for guiding the ball and loading pin. The polished and irradiated side of a TEM disk is placed face-down onto the circular recess of the die, and its perimeter is clamped by the clamping screw. Then, a WC ball of 1 mm diameter is placed on the top of the TEM disk, and a load is applied on the WC ball by the plunger. Displacements were measured using two linear variable differential transducers (LVDTs). One LVDT is attached to the cross head of the tensile machine to measure the displacement of the WC ball, and the other is placed under the TEM disk, touching the bottom face of the disk. Disk bend testing was performed at room temperature at a cross-head speed of 0.25 mm per minute, which gives a strain rate in the range of 10^{-3}–10^{-2} per second. Tensile testing was performed at a cross-head speed of 0.5 mm per minute, which equals a strain rate of 1.1×10^{-3} per second. All mechanical tests were carried out at room temperature.

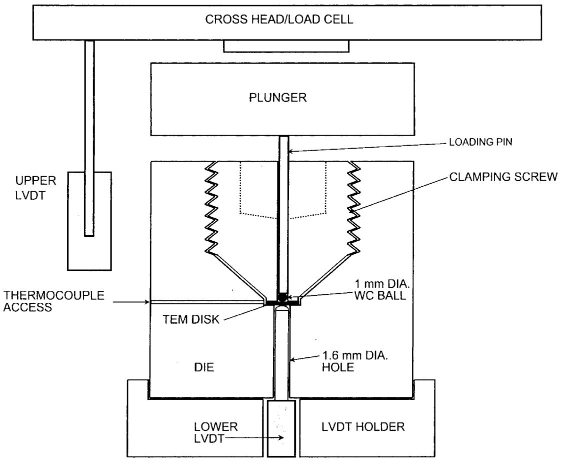

Fig. 1. Schematic illustration of disk bend test set-up.

In what follows it should be emphasized that Figs. 2–12 are for unirradiated disks. However, since the irradiated volume in the ion-irradiated disks is so small, the load–deflection results in these figures are virtually unaffected by irradiation. Figs. 13 and 14 show irradiation results.

TEM disks and tensile specimens of 316LN stainless steel were irradiated with 3.5 MeV Fe^+ ions at 200°C using a Van de Graaff accelerator at ORNL [16]. Irradiation with the 3.5 MeV Fe^+ ion beam produced a displacement damage profile having a maximum at a depth of 750–850 nm from the surface [15]. Detailed descriptions of the ion irradiation method and damage profile analysis have been published [16–18].

Table 1
Chemical compositions of test materials in wt%

Material	Fe	Ni	Cr	Mo	Mn	Si	C	N	Nb	V	W	Ta
Type 316LN austenitic stainless steel	Bal.	12.2	17.45	2.5	1.81	0.39	0.024	0.067	–	–	–	–
Fe–9Cr–2WVTa ferritic/martensitic steel	Bal.	<0.01	8.90	0.01	0.44	0.21	0.11	0.021	<0.01	0.23	2.01	0.06

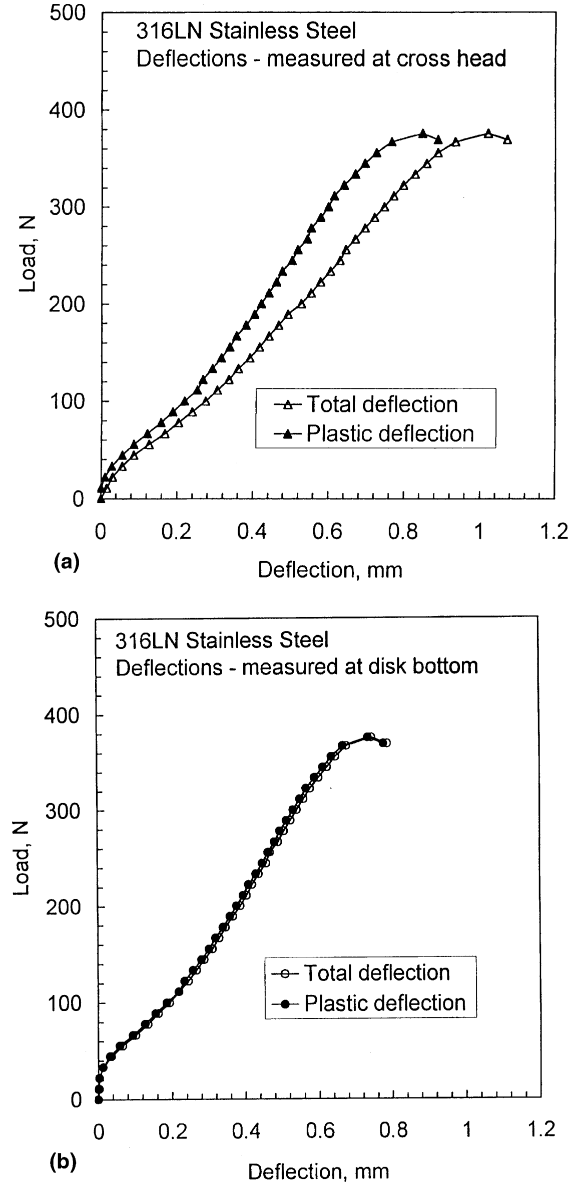

Fig. 2. Load versus deflection curves from the disk bend test for 316LN stainless steel; deflections were measured by (a) the LVDT in contact with the cross-head and (b) the LVDT placed under the specimen.

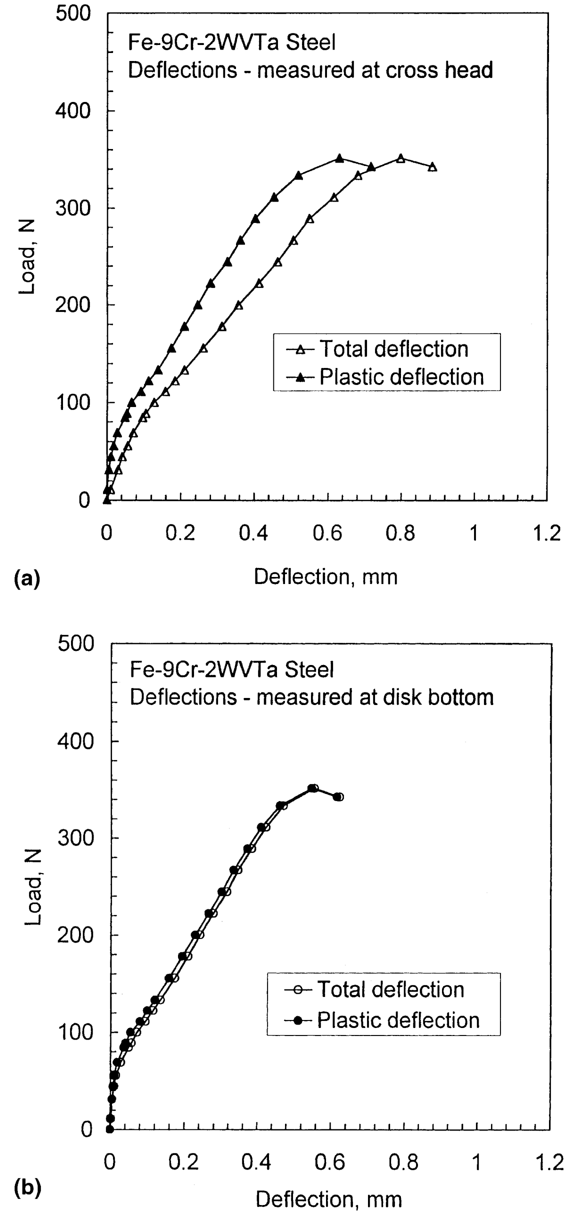

Fig. 3. Load versus deflection curves from the disk bend test of 9Cr–2WVTa ferritic/martensitic steel; deflections were measured by (a) the LVDT attached at the cross-head and (b) the LVDT placed under the specimen.

Slip line features of the irradiated surface (bottom surface in the test setup) were examined using an optical microscope after bending. The WC ball-contact surface (top surface) was also examined to determine the diameter of indentation impression and thus to be able to calculate the representative strain of the impression region. TEM microstructures after deformation were examined for both disk bend and tensile specimens. When preparing the TEM samples, the surface layer to a depth of about 600 nm was removed from the irradiated surface by electrochemical polishing followed by back thinning to perforation. This procedure allowed examination of the microstructure at the peak damage region between 600 and 800 nm depth from the original surface. Microstructures were examined in a Philips CM 12 transmission electron microscope at an acceleration voltage of 120 keV.

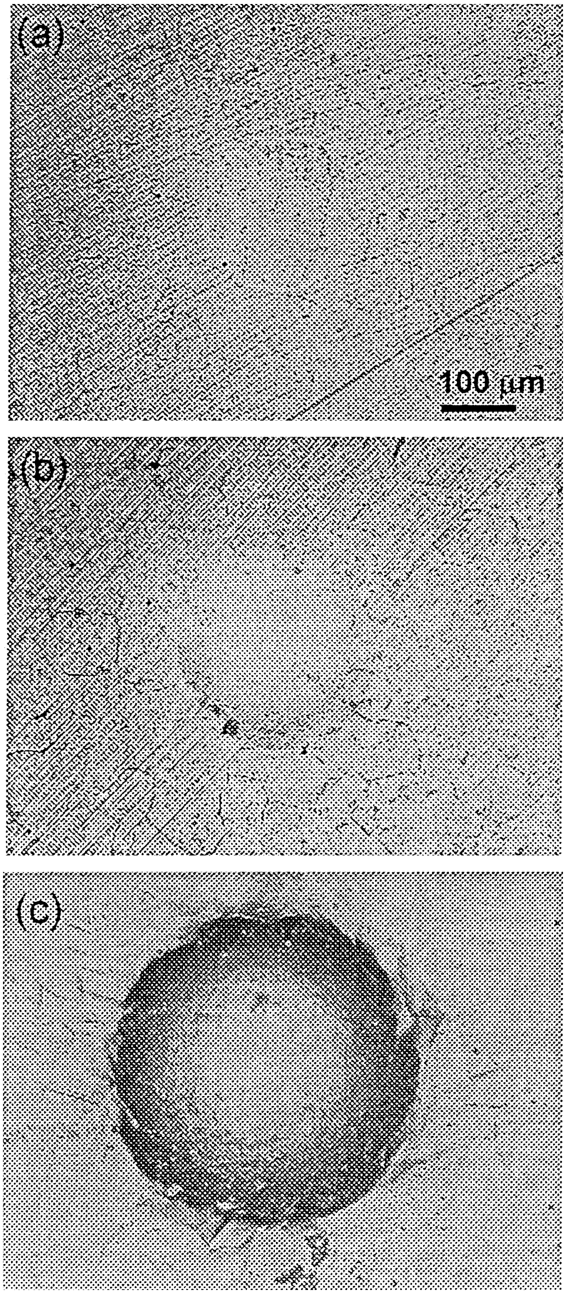

Fig. 4. Optical micrographs of indentation impressions on 316LN stainless steel after loading up to (a) 8 N($d_p = 179$ μm), (b) 26 N($d_p = 238$ μm), and (c) 50 N($d_p = 392$ μm).

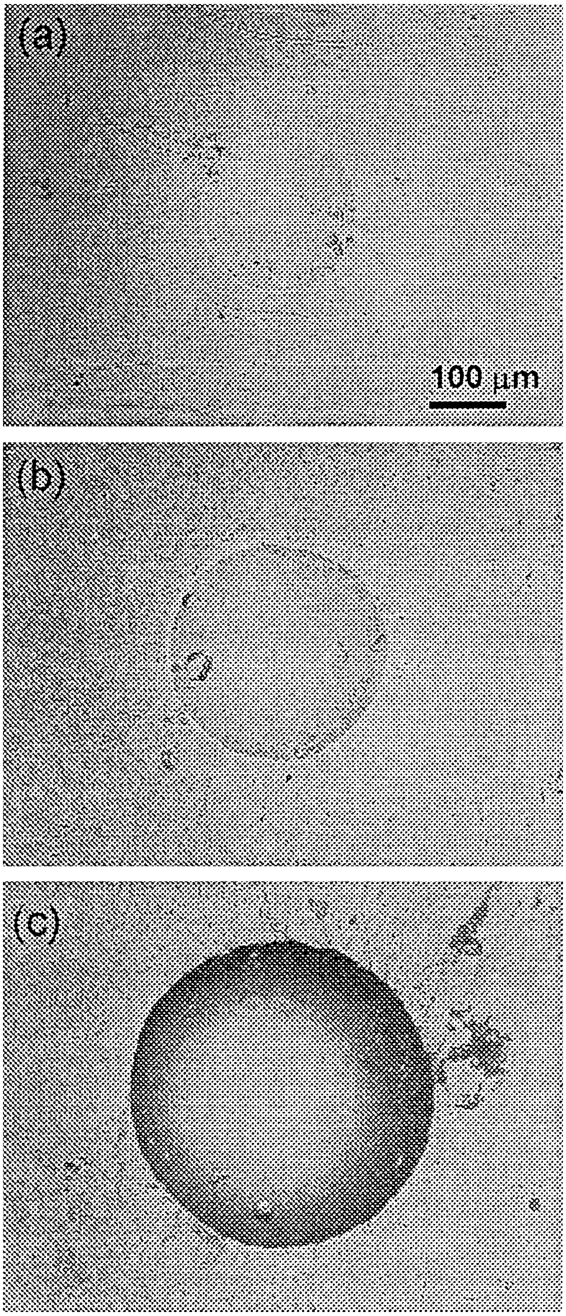

Fig. 5. Optical micrographs of indentation impressions in 9Cr–2WVTa ferritic/martensitic steel after loading up to (a) 39 N($d_p = 184$ μm), (b) 60 N($d_p = 252$ μm), and (c) 82 N($d_p = 349$ μm).

3. A method of evaluating deformation fields

3.1. Evaluation of plastic strains

A uniaxial loading during a disk bend test produces complex multiaxial strain fields within the specimen [1]. However, since the main purpose of this study is to characterize the deformation in the central region of the TEM disk, the analysis on the deformation fields is simplified by the geometrical symmetry in that region. Using a Cartesian coordinate system (x, y, z), ε^{p}_{xx}, ε^{p}_{yy}, and

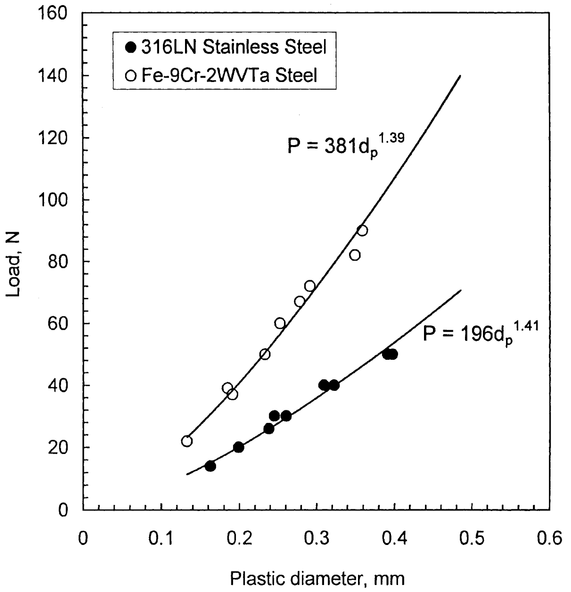

Fig. 6. Load versus indentation plastic strain diameter curves.

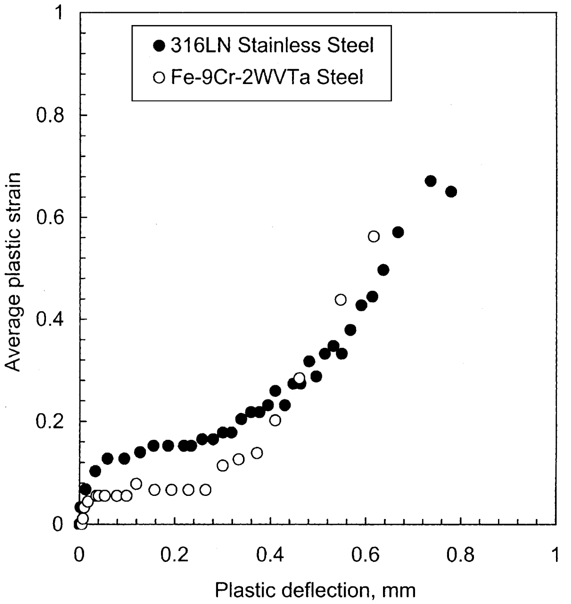

Fig. 7. Variation of average plastic strain with plastic deflection.

ε^{p}_{zz} are defined as the principal plastic strain components in the x-, y-, and z-directions, respectively. The z-direction is specified as the loading direction and x- and y-directions as the perpendicular directions. The average plastic strain in the z-direction is defined by [19]

$$\varepsilon^{p}_{zz} = \ln\left[\frac{\delta_0}{\delta_d}\right], \qquad (1)$$

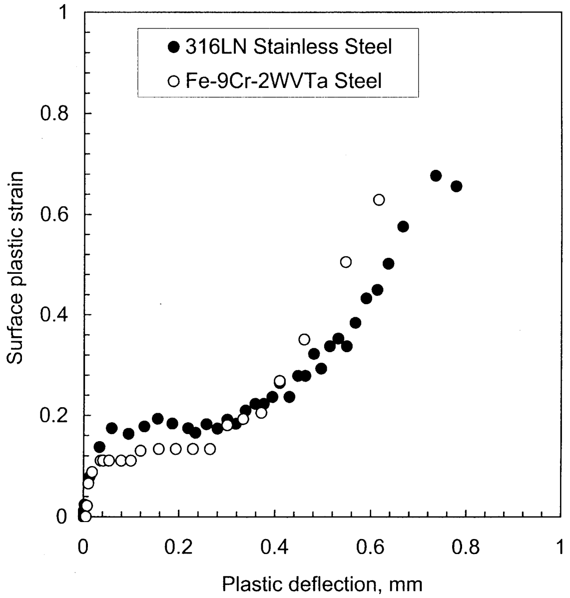

Fig. 8. Variation of surface plastic strain with plastic deflection.

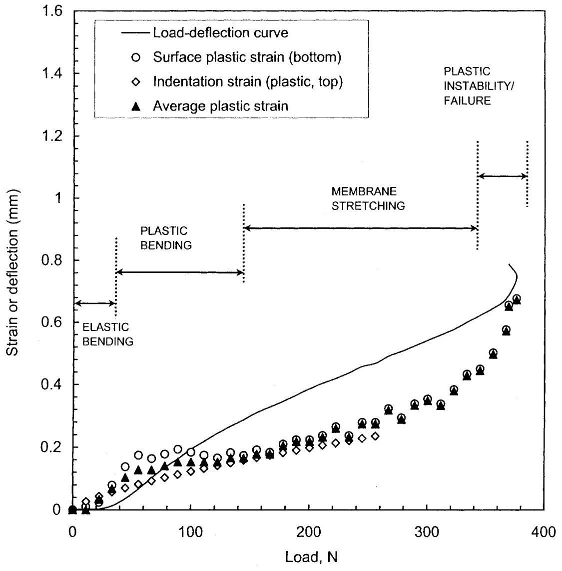

Fig. 9. Strain components and deformation regimes in the disk bend test for 316LN stainless steel.

where δ_0 and δ_d are the specimen thickness before and after deformation, respectively. Also, using the incompressibility condition, $\varepsilon^{p}_{xx} + \varepsilon^{p}_{yy} + \varepsilon^{p}_{zz} = 0$, geometrical symmetry, $\varepsilon^{p}_{xx} = \varepsilon^{p}_{yy}$, and equivalent strain, $\varepsilon^{p}_{eq} = (\sqrt{2}/3)[(\varepsilon^{p}_{xx} - \varepsilon^{p}_{yy})^2 + (\varepsilon^{p}_{yy} - \varepsilon^{p}_{zz})^2 + (\varepsilon^{p}_{zz} - \varepsilon^{p}_{xx})^2]^{1/2}$ [19], the following relationship is obtained for the plastic strain components:

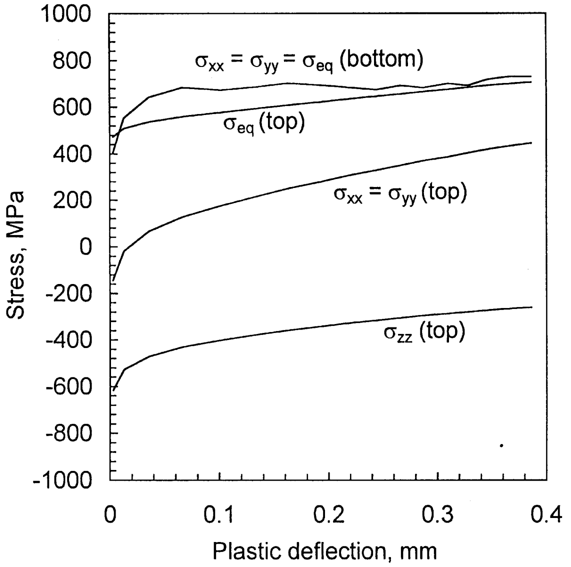

Fig. 10. Principal stress components in a 316LN stainless steel disk.

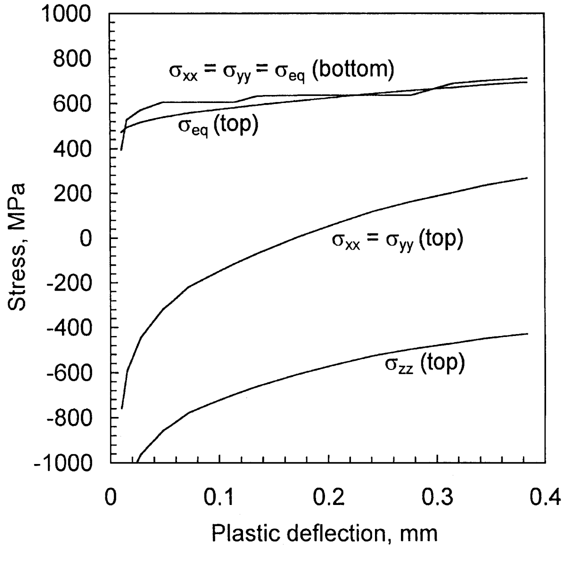

Fig. 11. Principal stress components in a 9Cr–2WVTa steel disk.

$$\varepsilon^{\mathrm{p}}_{xx} = \varepsilon^{\mathrm{p}}_{yy} = -\frac{1}{2}\varepsilon^{\mathrm{p}}_{zz} = -\frac{1}{2}\varepsilon^{\mathrm{p}}_{\mathrm{eq}}. \qquad (2)$$

It is known that the ductile disk bending consists of distinct deformation regimes: elastic bending, plastic bending, membrane stretching, and plastic instability and failure [1,8]. In the elastic bending regime, some plastic deformation occurs by indentation at the ball contact region but no significant plastic deformation is

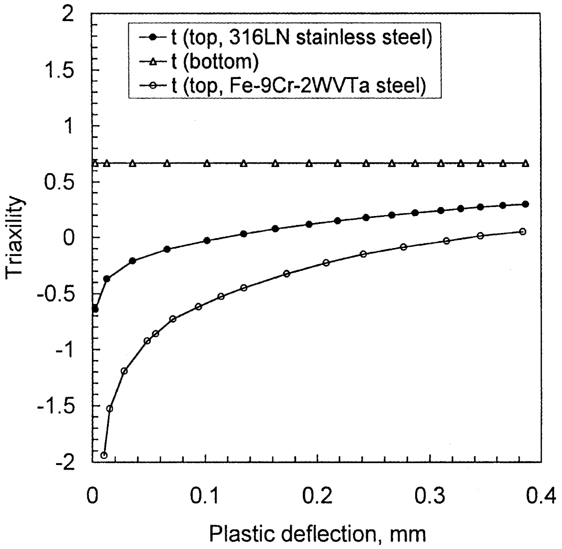

Fig. 12. Variation of stress triaxiality with deflection.

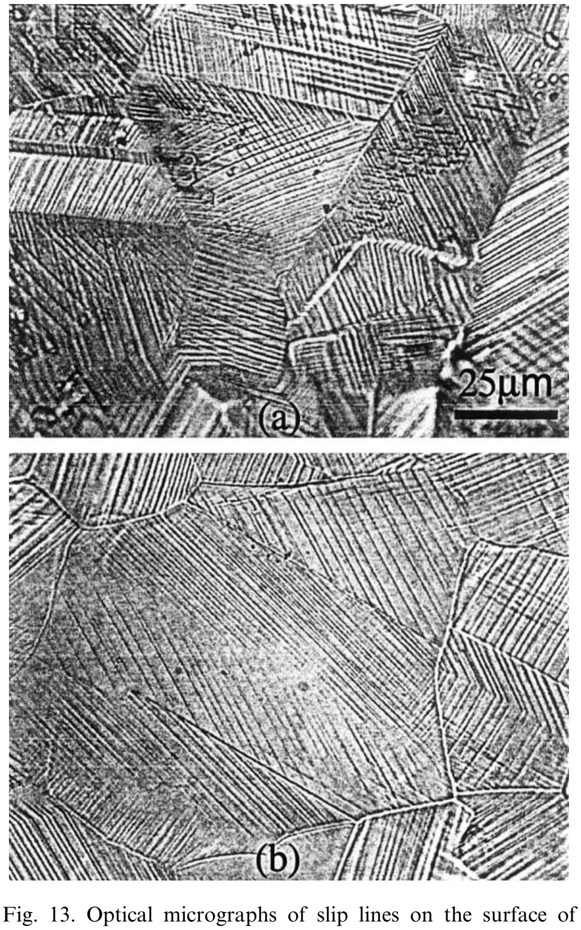

Fig. 13. Optical micrographs of slip lines on the surface of 316LN stainless steel after irradiation up to 10 dpa and about 10% plastic strain by (a) disk bend test and (b) tensile test.

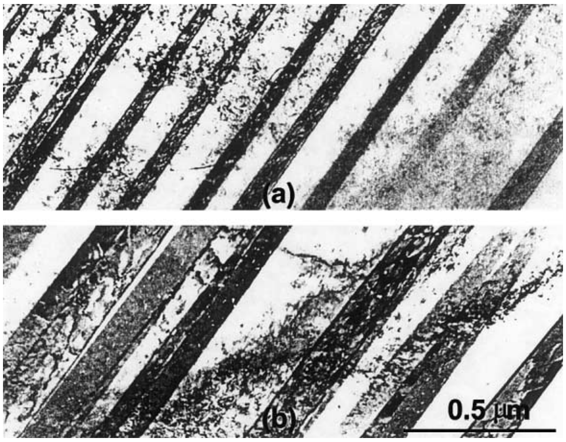

Fig. 14. TEM microstructures of 316LN stainless steel after irradiation up to 10 dpa and (a) about 10% plastic strain by disk bend test and (b) 20% plastic strain by tensile test.

produced at the bottom free surface. In the plastic bending regime, plastic deformation propagates to the bottom surface and some bulging develops at the bottom surface by bending deformation, following the contour of the ball (see Section 4.4 for detailed descriptions). In these initial deformation regimes, the indentation deformation at the top surface controls the deformation at the bottom surface where the material deforms due to bending. The ball indentation generates an impression at the top surface, and the strain at the impression can be evaluated from the measurements of the ball and impression diameters. This indentation strain has been called the 'representative strain' of the indentation impression [20–22]. Tabor developed an empirical relationship, in which the indentation (or representative) plastic strain, $\varepsilon_{\mathrm{I}}^{\mathrm{p}}$, is calculated from geometrical factors [20]:

$$\varepsilon_{\mathrm{I}}^{\mathrm{p}} = 0.2\frac{d_{\mathrm{p}}}{D}, \tag{3}$$

where d_{p} is the plastic diameter of the indentation impression and D is the ball diameter. For calculating the indentation strain, D is fixed at 1 mm (ignoring elastic deformation of the ball), and d_{p} is measured from an optical micrograph. Note that the compressive strains, $\varepsilon_{zz}^{\mathrm{p}}$ and $\varepsilon_{\mathrm{I}}^{P}$, are defined to be positive in the above equations after the conventional definitions [22]. Correspondingly, the signs of the other components, $\varepsilon_{xx}^{\mathrm{p}}$ and $\varepsilon_{yy}^{\mathrm{p}}$, are reversed, as indicated in Eq. (2).

Since the indentation is done from the top surface, a gradient in strain distribution through the specimen thickness exists. If a linear through-the-thickness distribution of plastic strain is assumed, the surface plastic strain at the bottom surface, $\varepsilon_{\mathrm{s}}^{\mathrm{p}}$, can be expressed as

$$\varepsilon_{\mathrm{s}}^{\mathrm{p}} = 2\varepsilon_{zz}^{\mathrm{p}} - \varepsilon_{\mathrm{I}}^{\mathrm{p}}. \tag{4}$$

This relationship is valid for the initial bending regimes where both the bending and indentation deformations are dominant. After the bending regimes, the disk deforms mainly by membrane stretching [1]. As discussed in Section 4.3, the plastic bending regime showed little increase in the plastic strain in the central region, while the plastic strain increased rapidly during the membrane–stretching regime. In this membrane–stretching regime, the plastic strain due to indentation and bending remains almost constant, and the increment of total plastic strain occurs mainly due to stretching along the radial direction of the disk. In such a case, the strain increment in the central region is considered to be uniform throughout the disk thickness, and thus the following relationship is applicable:

$$\Delta\varepsilon_{\mathrm{s}}^{\mathrm{p}} = \Delta\varepsilon_{zz}^{\mathrm{p}}. \tag{5}$$

Here, $\Delta\varepsilon_{zz}^{\mathrm{p}}$ can be calculated from the measurements of thickness change by using Eq. (1).

3.2. Evaluation of stress components and stress triaxiality

During a uniaxial loading by ball indentation, symmetrical triaxial stress fields are generated in the central region of the disk [3,7]. Here, σ_{xx}, σ_{yy}, and σ_{zz} are defined as principal stress components in the x-, y-, and z-directions, respectively. On the top ball-contact surface, the stress in the z-direction, frequently called the contact pressure [20–22], can be obtained from the applied load, P, and the plastic diameter of indentation impression

$$\sigma_{zz} = -\frac{4P}{\pi d_{\mathrm{p}}^2} \tag{6}$$

at the top surface.

Note that the minus sign indicates that σ_{zz} is compressive at the top surface. Since at the center of the disk the stress fields are subjected to the condition of symmetry, the perpendicular components, σ_{xx} and σ_{yy}, are obtained for the top surface as follows:

$$\sigma_{xx} = \sigma_{yy} = \sigma_{\mathrm{eq}} + \sigma_{zz}. \tag{7}$$

Here, the equivalent stress, σ_{eq}, is defined by [19]

$$\sigma_{\mathrm{eq}} = \frac{1}{\sqrt{2}}[(\sigma_{xx} - \sigma_{yy})^2 + (\sigma_{yy} - \sigma_{zz})^2 + (\sigma_{zz} - \sigma_{xx})^2]^{1/2}. \tag{8}$$

The value of σ_{eq} at a given plastic strain was calculated using an empirical tensile flow curve for each material; $\sigma_{\mathrm{eq}} = K(\varepsilon_{\mathrm{eq}}^{\mathrm{p}})^n$, where K and n are the strength coefficient and strain-hardening exponent of the power-law curve, respectively.

At the bottom surface of the disk, the stress component in the surface-normal direction does not exist; i.e.,

$$\sigma_{zz} = 0 \tag{9}$$

at the bottom surface.

Then the perpendicular stress components for the bottom surface are given by

$$\sigma_{xx} = \sigma_{yy} = \sigma_{\mathrm{eq}}. \tag{10}$$

Finally, the stress state can be expressed in terms of the above stress components. Here, the qualitative stress state is expressed by the stress triaxiality, t, defined as the ratio of the mean stress, $\sigma_m = (\sigma_{xx} + \sigma_{yy} + \sigma_{zz})/3$, to the equivalent stress, σ_{eq} [25,26]:

$$t = \frac{\sigma_m}{\sigma_{\mathrm{eq}}}. \tag{11}$$

Using the preceding expressions for stress components, the stress triaxialities are derived for the top and bottom surfaces, t_{T} and t_{B}, respectively, as

$$t_{\mathrm{T}} = \frac{2}{3} - \frac{4P}{\pi d^2 \sigma_{\mathrm{eq}}} \tag{12}$$

and

$$t_{\mathrm{B}} = \frac{2}{3}. \tag{13}$$

4. Results and discussion

4.1. Load–deflection curves

The load–deflection curves are plotted for 316LN and 9Cr–2WVTa steels in Figs. 2(a) and (b) and 3(a) and (b), respectively, in which the applied load is plotted against total (elastic + plastic) and plastic deflections. The initial parabolic portion in the load–deflection curves is called the bending regime and the next linear portion the stretching regime, which is followed by a plastic instability/failure regime [1,8]. As will be discussed in detail in Section 4.4, the load–deflection curves of both test materials obey the conventional pattern of deformation regimes in the ductile disk bending.

As seen in Figs. 2(a) and 3(a), large elastic deflections, the difference between the total deflection and the plastic deflection, were seen when the deflections were recorded from the upper LVDT attached to the cross head of the testing machine. However, the elastic deflections from the lower LVDT touching the bottom of the specimen were insignificant as seen in Figs. 2(b) and 3(b). Although elastic deflections are expected in all the components of the test system, the large elastic deflections in Figs. 2(a) and 3(a) seem to originate mostly from the system compliance, namely elastic deformation of the loading pin of 1 mm diameter and 25 mm length. This pin was made of a tool steel and has the smallest ratio of cross-section to length in the test set-up. In the following sections, therefore, only the plastic deflection measurements are used in evaluating strain and stress data.

4.2. Indentation deformation at disk specimen

Optical micrographs in Figs. 4 and 5 illustrate the growth of indentation impressions during the disk bend tests for 316LN and 9Cr–2WVTa steels, respectively. For both test materials the diameter of the impression increases as the applied load increases. According to the indentation deformation models [20,21], the representative strain around the impression is determined by the geometrical factors of the impression and strains up to 20% can be produced by the ball indentation as indicated in Eq. (3). Although most authors have paid little attention to the role of indentation deformation in the bending deformation [1–14], the present results indicate that the indentation strain may be important in most strain ranges.

Fig. 6 presents the relationships between the plastic diameter and the indentation load for 316LN and 9Cr–2WVTa steels, in which regression curves are also shown. In the next section, these curves are used for calculating the indentation strain at a given load. Note that the exponents of the regression curves in Fig. 6 are lower than those of indentation tests on bulk specimens [23,24]. The Meyer law [20] describes the relationship between the load and the impression diameter as $P = kd_{\mathrm{p}}^{\mathrm{m}}$, where k is a proportionality constant and the exponent m is the Meyer index. A number of indentation test results found that the exponent m was close to the value of $n + 2$ [20], where n is the strain hardening exponent of uniaxial tensile curve. Since the n-values for 316LN and 9Cr–2WVTa steels are about 0.3 and 0.1, respectively, the corresponding m-values would be about 2.3 and 2.1. However, the measured exponents from the curves in Fig. 6 are 1.41 and 1.39. These lower values are due to the absence of supporting substrate at the bottom side of the disk.

4.3. Plastic strain

Fig. 7 presents the variation of average plastic strain, $\varepsilon_{zz}^{\mathrm{p}}$, with deflection; where the strain values were calculated from the thickness reduction measurements by using Eq. (1). Both 316LN and 9Cr–2WVTa steels showed nearly constant strains in a deflection region of 0.05–0.3 mm after a rapid increase of strain at the beginning of deflection; those constant strains were about 15% for 316LN stainless steel and about 7% for 9Cr–2WVTa steel. As will be discussed in the next section, this constant strain region corresponds to the plastic bending regime. In this regime, the bending deformation spreads out in the radial direction from the center of the disk with most plastic deformation occurring in the bulged region under the ball contact area. Since the bending curvature of the bulged region was almost constant during plastic bending, the plastic strain measured at the center of the disk showed little change.

After this near-constant strain region, the average plastic strain started to increase rapidly until plastic instability and/or fracture set in. The rapid increase of strain in this region was due to the plastic flow in the radial direction, and this plastic deformation is thus called the membrane-stretching deformation. It is also noted that the plastic strain rate was higher for 9Cr–2WVTa steel than for 316LN stainless steel. This was mainly because of the earlier deformation localization in the 9Cr–2WVTa steel due to its lower strain-hardening capability.

Since ion beam-induced microstructures are limited to the surface layer, the surface plastic strains were determined by using Eqs. (4) and (5). The results are plotted in Fig. 8. The shapes of the surface plastic strain versus plastic deflection curves were similar to those shown in Fig. 7. However, the surface strains in the plateau region were slightly higher than the average plastic strains in Fig. 7: about 18% for 316LN stainless steel and about 12% for 9Cr–2WVTa steel.

4.4. Deformation regime

For ductile metals, many investigators [1,8] have reported that there exist distinct deformation regimes in the disk bend deformation, namely elastic bending, plastic bending, membrane stretching, and plastic instability/failure regimes. These regimes can be seen in the load–deflection curves measured at the center of the disk as in Figs. 2 and 3. Fig. 9 shows the corresponding deformation regimes in the strain components; both the average plastic strain and the surface plastic strain reveal well-defined deformation regimes. It is noted that the transitions between deformation regimes are more distinct in the plastic strains than in the load–deflection curves.

The first deformation mode in the disk bending is elastic bending. The steep and almost linear portion on the initial load–deflection curve belongs to this regime. A finite element analysis on strain contours by Manahan et al. [1] revealed that the specimen yields shortly after contact with the indenter in a localized region near the contact point. Also, it is known that the maximum equivalent stress is obtained at an interior position beneath the ball contact area and that the yielding started from that position propagates through the thickness and radially outward over the disk [1]. During this elastic bending regime, elastic deformation is dominant in most parts of the disk except for the ball contact area. The plasticity in the deflection originates mostly from the ball indentation deformation.

When the yield surface reaches the bottom surface of the disk, plastic bending commences [1,8], extruding the central area of the bottom surface. As the plastic deformation spreads outward, the top surface of the disk wraps around the ball. We observed that most plasticity occurred only at a limited volume under the ball contact area. Since the plastic strain in the central region is determined mainly by geometrical parameters such as the ball size, specimen thickness, and test configuration, the plastic strain at the center of the disk shows little change during this deformation stage. The hardening rates in the load–deflection curves are relatively low in this stage.

Since most plasticity is limited to a small volume under the ball in the plastic bending regime, plastic bending alone cannot account for the large deflection after the plastic bending regime. At this stage, a transition from bending to membrane stretching occurs. This transition is characterized by the change in the load–deflection curve from parabolic to linear [1,8]. Figs. 2 and 3 show that the transition from plastic bending to membrane stretching in the load–deflection curves occurs progressively over a deflection range. Sometimes the transition region is defined as a separate deformation regime [1]. In Figs. 7 and 8, however, the plastic strains show more distinct transition; the membrane stretching occurs after a plastic deflection of about 0.3 mm. In the present study, the transition regime was included in the plastic bending regime, as indicated in Fig. 9.

In the membrane–stretching regime, radial plastic flow becomes dominant in most regions of the disk, and accordingly, rapid thickness reduction occurs. The tensile stress components become dominant, and the stress and strain distributions through the thickness become uniform as the plastic flow progresses. As indicated in Figs. 7 and 8, the maximum plastic strain due to bending is limited to a strain range of 10–20% due to geometrical constraints; however, the strain by the stretching deformation can increase to a higher level of 60–70% until plastic instability and fracture occur.

4.5. Stress components and stress state

Uniaxial tensile tests were performed for the test materials to obtain empirical flow curves and the curves were used for evaluating equivalent stress and stress components in the disk bend deformation. The empirical stress–strain curves were given as power-law equations: $\sigma_{\mathrm{eq}} = 1085\varepsilon_{\mathrm{p}}^{0.264}$ MPa for 316LN stainless steel and $\sigma_{\mathrm{eq}} = 966\varepsilon_{\mathrm{p}}^{0.105}$ MPa for 9Cr–2WVTa steel. In Figs. 10 and 11, the stress components are presented as a function of plastic deflection for both top and bottom sides of the disks. At the center of the top surface, the equivalent stress is always tensile, while the stress in the *z*-direction (loading direction) is compressive, as defined in Eqs. (6) and (8). The principal stress components in the perpendicular (x and y) directions change their sign from compressive to tensile during deformation. When the perpendicular components increase to high tensile values, the disk deforms mainly by stretching. Fig. 11 shows also that the 9Cr–2WVTa steel shows much higher compressive stresses at an early stage of deformation due to its high strength.

At the center of the bottom surface, on the other hand, the equivalent stress and two perpendicular stress components have the same values and are always tensile, as indicated in Eq. (10). In this case the stress state is perfectly biaxial.

Fig. 12 presents the variations of stress triaxialty for the two test materials. For both materials, the triaxiality at the top surface increases from negative to positive, while a constant value of 2/3 is calculated for bottom surfaces of both materials. This means that a dramatic change in stress field occurs through a small specimen thickness of about 0.25 mm. Table 2 compares the stress states evaluated for various specimen configurations. Here, it should be noted that the degree of constraint in deformation depends only on the absolute value of the stress triaxiality [23,24]. The highest degree of constraint is expected in the deformations at a crack tip and for ball indentation. Note that the stress triaxiality on the bottom surface of a TEM disk is similar to the values in necked tensile specimens, either diffuse neck or localized neck. Further, uniform deformation in uniaxial tensile testing has a low triaxiality of 1/3, and the stress triaxiality on the bottom surface of a disk is 2/3, which is not affected by irradiation. The factor of two difference between these values is relatively small when compared to the larger values of triaxiality in a ball indentation or at a crack tip. No change in deformation mechanism due to this difference in stress state has been reported [8]. Also, in polycrystalline materials, the interactions between adjacent grains produce multiaxial local stress fields under uniaxial loading, so the individual grains are already subjected to a multiaxial stress state. Therefore, it is expected that the different stress states of disk bend deformation at the bottom surface and uniaxial tensile deformation lead to similar deformation mechanisms.

4.6. Comparison of microstructures

Fig. 13 compares optical micrographs of slip lines on the surfaces of 316LN stainless steel specimens irradiated with Fe^+ ions up to 10 dpa. The slip lines were formed by about 10% strain in the disk bend test and uniaxial tensile test. Both micrographs show that slip lines were mostly straight, and that multiple slip occurred during deformation. The density and direction of slip lines varied even within the same grain as well as from grain to grain. It was also observed that annealing twins became more distinct due to a change in direction of the slip lines at the twins.

Although overall slip line features were qualitatively similar for the two deformations, it was recognized that the slip line density and grain distortion at the disk surface were higher than those at the tensile specimen surface. This can be explained by a confinement effect of slip lines in the disk bend test. In the uniaxial tensile deformation, any 45° direction from the loading axis can be a most probable slip direction. Thus dislocation slip lines can appear at any free surfaces of the gauge section. In the disk bend deformation, however, the dislocation glide direction must include a vector component that is normal to the top or bottom surfaces and the slip lines appear only at those surfaces. Since the slip lines can not be formed at the ball contact area, most dislocation glide may be released to the bottom surface. Therefore, the density of slip lines at the bottom surface of the disk is higher than that at the tensile specimen surface.

TEM microstructures in Fig. 14 also indicate that the deformation microstructures of disk bend and uniaxial tensile tests are qualitatively similar. Both TEM micrographs show radiation damage structures, twin bands formed by partial dislocation glide [15,28], and some tangled dislocations. There was no evidence that any different deformation mechanisms were operating in the two different testing modes.

Table 2
Some stress triaxiality (t) values in the various specimen configurations

Specimen type	Position	Material	Stress state	t (absolute values)	References
Disk bend	Center of Convex surface	All materials	Biaxial	0.67	Present study
	Center of concave (ball-contact) surface	316LN	Triaxial	0–0.9	Present study
		9Cr–2WVTa		0–1.8	
Round tensile	Uniform region	All materials	Uniaxial	0.33	[23]
	Necked region	SA508-3	Triaxial	0.33–0.8	[23,24]
Plate tensile	Uniform region	All materials	Uniaxial	0.33	Present study
	Localized neck	All materials	Biaxial	0.58	Present study
Compact tension	Crack tip	SA508-3	Triaxial	1.9–2.8	[27]
Ball indentation	Center of impression	SA508-3	Triaxial	1.9–3.0	[23,24]

5. Summary and conclusion

A theoretical and experimental basis for a disk bend test method was established to study deformation mechanisms and mechanical properties. The stress and strain fields generated during disk bend tests were evaluated for 316LN and 9Cr–2WVTa steels. Both materials showed nearly constant average plastic strain and surface plastic strain in the plastic bending regime, and these increased rapidly in the subsequent stretching regime. The deformation regimes of the plastic strain versus deflection curves corresponded to those of the load versus deflection curves.

The stress components were also analyzed for disk specimens of the two test materials. On the top surface of the disk, the stress in the loading direction was compressive during bending deformation, and the perpendicular stress components varied from negative to positive. The stress triaxiality on this top surface had negative values initially, but increased with deflection. On the free bottom surface, the two perpendicular stress components were always positive, while the component in the surface normal direction was set to zero. A constant stress triaxiality of 2/3 was calculated for this bottom surface, which was very similar to the values in the necked region of uniaxial tensile specimens.

Optical and TEM micrographs from both disk and tensile specimens showed similar slip line features, but the disk specimen showed higher slip line density. The microstructural evidence suggested that the deformation mechanisms were similar for disk bend and tensile tests.

The above results suggest that the miniaturized disk bend technique can be used for studying deformation mechanisms, and that the results would be similar to those from a uniaxial tensile test. Although this technique was developed for irradiated materials, it is also applicable to unirradiated materials.

Acknowledgements

This research was sponsored by the Division of Materials Sciences and Engineering, US Department of Energy, under contract DE-AC05-00OR22725 with UT-Battelle, LLC.

References

[1] M.P. Manahan, A.E. Browning, A.E. Argon, O.K. Harling, in: W.R. Corwin, G.E. Lucas (Eds.), The Use of Small Scale Specimens for Testing Irradiated Material, ASTM STP 888, Philadelphia, PA, 1986, p. 17.

[2] R.L. Klueh, D.N. Braski, in: W.R. Corwin, G.E. Lucas, (Eds.), The Use of Small Scale Specimens for Testing Irradiated Material, ASTM STP 888, Philadelphia, PA, 1986, p. 66.

[3] M.L. Hamilton, F.H. Huang, in: W.R. Corwin, G.E. Lucas (Eds.), The Use of Small Scale Specimens for Testing Irradiated Material, ASTM STP 888, Philadelphia, PA, 1986, p. 5.

[4] F.H. Huang, M.L. Hamilton, G.L. Wire, Nucl. Technol. 57 (1981) 234.

[5] O.K. Harling, M. Lee, D.-S. Sohn, G. Kohse, C.W. Lau, in: W.R. Corwin, G.E. Lucas (Eds.), The Use of Small Scale Specimens for Testing Irradiated Material, ASTM STP 888, Philadelphia, PA, 1986, p. 50.

[6] M.L. Hamilton, M.B. Toloczko, G.E. Lucas, in: P. Jung, H. Ullmaier, Jòlich (Eds.), Miniaturized Specimens for Testing of Irradiated Materials, 1995, p. 46.

[7] G.E. Lucas, G.R. Odette, J.W. Sheckherd, in: W.R. Corwin, G.E. Lucas (Eds.), The Use of Small Scale Specimens for Testing Irradiated Material, ASTM STP 888, Philadelphia, PA, 1986, p. 112.

[8] X. Mao, J. Kameda, J. Mater. Sci. 26 (1991) 2436.

[9] X. Mao, H. Takahashi, T. Kodaira, Scripta Met. Mater. 25 (1991) 2487.

[10] Y.H. Joo, T. Hashima, H. Takahashi, JTEVA 20 (1992) 6.

[11] J.R. Foulds, R. Viswanathan, J. Eng. Mater. Technol. 116 (1994) 457.

[12] J.R. Foulds, P.J. Woytowitz, T.K. Parnell, C.W. Jewett, JTEVA 23 (1995) 3.

[13] G.L. Hankin, M.L. Hamilton, F.A. Garner, R.G. Faulkner, Shear Punch Testing of ^{59}Ni Isotope-doped Model Austenitic Alloys after Irradiation in FFTF at Different He/DPA Ratios, Pacific National Northwest Lab., Richland, WA, PNL-SA-28594, 1997.

[14] G.L. Hankin, M.M., Toloczko, M.L. Hamilton, R.G. Faulkner, Validation of the Shear Punch-Tensile Correlation Technique Using Irradiated Materials, Pacific National Northwest Laboratory, Richland, WA, PNL-SA-28629, 1997.

[15] E.H. Lee, T.S. Byun, J.D. Hunn, N. Hashimoto, K. Farrell, J. Nucl. Mater. 281 (2000) 65.

[16] M.B. Lewis, W.R. Allen, R.A. Buhl, N.H. Packan, S.W. Cook, L.K. Mansur, Nucl. Instrum. and Meth. B 43 (1989) 243.

[17] J.F. Ziegler, J.P. Biersack, U. Littemark, The Stopping and Range of Ions in Solids, Pergamon, New York, 1985.

[18] E.H. Lee, Nucl. Instrum. and Meth. B 151 (1999) 29.

[19] G.E. Dieter, Mechanical Metallurgy, 3rd Ed., McGraw-Hill, New York, 1986, pp. 88 and 506.

[20] D. Tabor, J. Inst. Met. 79 (1951) 1.

[21] H.A. Francis, J. Eng. Mater. Technol. 98 (1976) 272.

[22] T.S. Byun, J.H. Hong, F.M. Haggag, K. Farrell, E.H. Lee, Int. J. Press. Vessel Piping 74 (1998) 231.

[23] T.S. Byun, J.W. Kim, J.H. Hong, J. Nucl. Mater. 252 (1998) 187.

[24] T.S. Byun, S.H. Kim, B.S. Lee, I.S. Kim, J.H. Hong, J. Nucl. Mater. 277 (2000) 263.

[25] M.S. Mirza, D.C. Barton, P. Church, J. Mater. Sci. 31 (1996) 453.

[26] A.C. Mackenzie, J.W. Hancock, D.K. Brown, Eng. Frac. Mech. 9 (1977) 167.

[27] H. Kordisch, E. Sommer, W. Schmitt, Nucl. Eng. Design 112 (1989) 27.

[28] C. Bailat, F. Groschel, M. Victoria, J. Nucl. Mater. 276 (2000) 283.